

Crystallographic, Structural and Band Gap Tailoring of $\text{Zn}_{0.98}\text{Mn}_{0.02}\text{S}$ Quantum Dots Co-Doped with Cu by Co-Precipitation Method

P. Sakthivel¹ · S. Muthukumar²

Received: 18 December 2015 / Accepted: 5 February 2016 / Published online: 12 February 2016
© Springer Science+Business Media New York 2016

Abstract $\text{Zn}_{0.98-x}\text{Cu}_x\text{Mn}_{0.02}\text{S}$ ($x = 0, 0.02, 0.04$) quantum dots with different Cu concentrations have been successfully synthesized by co-precipitation method. Cubic phase exhibited in $\text{Zn}_{0.98}\text{Mn}_{0.02}\text{S}$ turned to mixture of both cubic and hexagonal phases by Cu-doping which was confirmed by X-ray diffraction pattern. The shift of peak position along (111) plane and the diminishing of interplanar distance and lattice constant confirmed the proper substitution of Cu and Mn in ZnS. Cubic phase of ZnS was tuned towards hexagonal phase by Cu-doping i.e., morphology diminishes stability which was confirmed by microscopic images. Optical studies revealed the wide tuning of band gap between 3.3 and 3.93 eV by Mn-doping and Cu co-doping which is useful for opto-electronic device applications. Photoluminescence spectra illustrated two distinct emission bands, UV emission around 392–396 nm and defect related blue emission around 470–481 nm. The change in intensity and peak position of UV and blue emission was discussed based on crystallite size formation of defect states by Cu-doping.

Keywords Mn, Cu co-doped ZnS · Co-precipitation · X-ray diffraction · SEM · Band gap tailoring · Photoluminescence

1 Introduction

In recent years, semiconducting quantum dots (QDS) is being a interesting one due to their structural, electronic and optical properties [1]. Energy gap of these QDs can be simply modified by minor adjustment in size and composition of materials [2]. The peculiar properties of QDs make them useful for the applications like imaging, sensors, phototonics, solar cell, etc. [3, 4].

Among different II–VI type semiconductors ZnS (Energy gap ~ 3.66 at 300 K) is significant one because of its optoelectronic and luminescence device applications [5, 6]. Plenty of researchers have examined the optical, microstructural and luminescent properties of doped ZnS nanostructures [7], particularly Mn-doped ZnS nanoparticles [8, 9]. When Mn^{2+} ions are substituted instead of Zn^{2+} in ZnS, they showed green, orange and red photoluminescence upon UV radiation [10, 11] that's why they have been extensively applied as phosphors for displays and lamps. Bhargava and Gallagher [12] described that the PL of Mn^{2+} doped ZnS nanoparticles have improved the quantum efficiency compared to the bulk form. Since the higher percentage of Mn concentration induces secondary phase formation and Mn = 2 % doped ZnS has higher transmittance [13], Mn content in the present study is limited to 2 %.

Co-doping may change the materials properties such as magnetic properties, the mobility, the type and the concentration of charge carriers. Yang et al. [14] noticed the prominent and stable visible-light emission from 515 to 560 nm at room temperature in Co^{2+} and Cu^{2+} co-doped ZnS nanocrystals. Among the different transition metals (TM), Cu-doped ZnS QDs attract extraordinary attention due to the highly effective luminescence [12]. Recently, Mn, Cu co-doped nanoparticles have paying much interest

✉ S. Muthukumar
drsmk123@yahoo.co.in

¹ Mount Zion College of Engineering & Technology,
Pudukkottai, Tamil Nadu 622507, India

² PG & Research Department of Physics, Government Arts
College, Melur, Tamil Nadu 625106, India

in research due to its multi-functions by transporting and controlling numerous types of spin state [15, 16].

In the present work, an attempt has been made to synthesize the Cu co-doped $Zn_{0.98}Mn_{0.02}S$ doped ZnS QDs with Cu = 0, 2 and 4 % by simple co-precipitation method because it is one of the important inexpensive and more yielding producing method [17]. The role of Cu on structure, size, structure, morphology and photoluminescence properties of the resulting $Zn_{0.98-x}Cu_xMn_{0.02}S$ ($x = 0, 0.02$ and 0.04) QDs were studied and discussed with their effects.

2 Experimental

2.1 Materials

Zinc acetate ($Zn(CH_3COO)_2 \cdot 2H_2O$, source of Zn^{2+} , anions) and sodium sulfide (Na_2S , source of S^{2-} , cations) were taken as the precursors. Manganese acetate ($Mn(CH_3COO)_2 \cdot 2H_2O$, source of Mn^{2+} , anions) and copper acetate ($Cu(CH_3COO)_2 \cdot 4H_2O$, source of Cu^{2+} , anions) were chosen as dopant materials. Aqueous ammonia solution was used to change the pH of the solution. All the chemicals used in the present were in analytical grade (AR) with 99.99 % purity purchased from M/s. Merck. Ultra pure de-ionized water was used as solvent throughout the synthesis process.

2.2 Preparation of $Zn_{0.98-x}Cu_xMn_{0.02}S$ ($x = 0, 0.02$ and 0.04) Quantum Dots

The source materials were weighed by using high sensitive electronic balance for the intentional addition of dopant with desired ratio. For the preparation of $Zn_{0.96}Cu_{0.02}Mn_{0.02}S$ quantum dots, 0.96 M zinc acetate, 0.02 M manganese acetate 0.02 M copper acetate were gradually dissolved (one by one) in 50 ml double distilled water and kept at constant stirring (at rate of 1000 rpm) at 80 °C until a clear and homogeneous solution is obtained. Then, 50 ml 1 M sodium sulfide solution was added drop by drop to the above mixture solution under continuous stirring for 8 h. Aqueous ammonia solution was used to maintain the pH Value of the mixer solution as 9.5.

The composition of Cu^{2+} was adjusted by controlling the quantity of copper acetate in the above solution. After 8 h, a light gray to dark gray precipitate was deposited at the bottom of the flask. The wet precipitate was filtered out separately and washed with de-ionized water and methanol to remove unwanted impurities formed during the preparation process. Finally, obtained product was dried using micro-oven at 50–80 °C for 5 h. The final precipitates were grounded using an agate mortar. The same procedure was

repeated to get $Zn_{0.98-x}Cu_xMn_{0.02}S$ QDs with various composition of Cu. The doping concentration of Mn was fixed as 0.02 and Cu varied as 0, 0.02 and 0.04. Hereafter, $Zn_{0.96}Cu_{0.02}Mn_{0.02}S$ and $Zn_{0.94}Cu_{0.04}Mn_{0.02}S$ samples were termed as ZCM-2 and ZCM-4, respectively.

2.3 Characterization

The crystal structure of $Zn_{0.98-x}Cu_xMn_{0.02}S$ ($x = 0, 0.02, 0.04$) QDs were examined by powder X-ray diffractometer. The diffracted patterns were recorded by RigaKuC/max-2500 diffractometer using CuK α radiation ($\lambda = 1.5406 \text{ \AA}$) at 40 kV and 30 mA from $2\theta = 20^\circ$ to 70° with scan rate 0.1° per min. The surface morphology of the synthesized QDs was studied using scanning electron microscope (SEM, JEOLJSM 6390). All the characterizations were carried out at room temperature.

The UV–visible optical absorption and transmittance studies were carried out to investigate their optical properties using UV–visible spectrometer (Model: Lambda 35, Make: Perkin Elmer) from 300 to 600 nm at ambient temperature. Halogen and deuterium lamps were used as sources for visible and UV radiations, respectively. The presence of chemical bonding was studied by fourier transform infra-red (FTIR) spectrometer (Model: Perkin Elmer, Make: Spectrum RXI) from 400 to 4000 cm^{-1} . Pellets were prepared by mixing the nanoparticles with KBr at 1 wt%. Room-temperature photoluminescence (PL) measurements have been carried out using (Model: Hitachi, Make: F-2500) at excitation wavelength of 330 nm and power of 150 W in order to study the radiative recombination properties.

3 Results and Discussion

3.1 XRD—Structural Analysis

X-ray diffraction has been used to examine the result of Cu doping on the structure of $Zn_{0.98}Mn_{0.02}S$ QDs. The result of Mn alone and simultaneous doping of Mn and Cu with different composition of Cu = 0, 0.02 and 0.04 on the structure and the phase composition of ZnS are shown in Fig. 1. XRD patterns were recorded over the range of 20° to 70° . The XRD pattern of $Zn_{0.98}Mn_{0.02}S$ QDs shows three well defined diffraction peaks matching with the lattice planes (111), (220) and (311) where (111) plane has favoured orientation among all the planes. The observed major diffraction peaks matched well with the JCPDS no. (80-0020) corresponding to cubic structure (zinc blende) of ZnS. No extra peaks noticed from XRD pattern related to Zn/Mn impurities confirm the phase purity of the sample. The higher full width at half maximum (FWHM) value

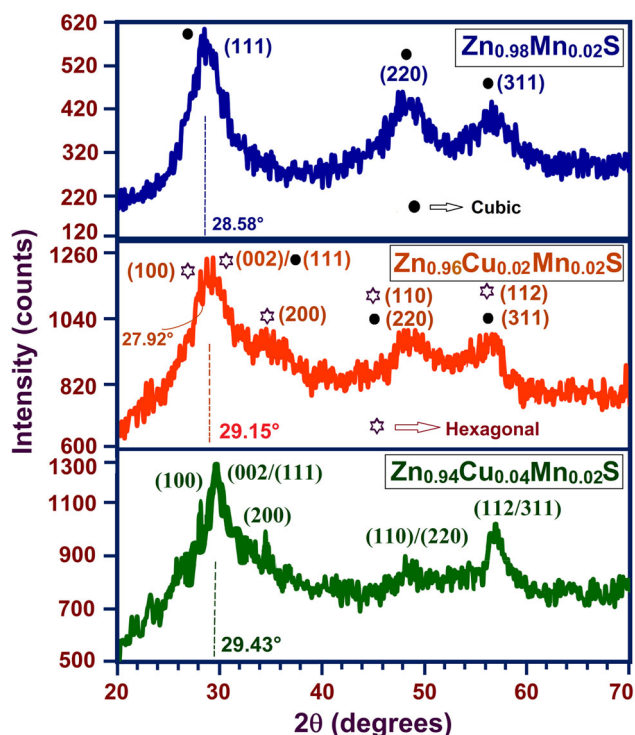


Fig. 1 X-ray diffraction patterns of $\text{Zn}_{0.98-x}\text{Cu}_x\text{Mn}_{0.02}\text{S}$ ($x = 0, 0.02$ and 0.04) QDs

observed in the sample designate the nanocrystalline nature of the samples.

The more intense peak along (111) plane is shifting towards higher angle side when Cu is substituted into Zn–Mn–S. The observed shift in peak position as noticed from Fig. 1 is appropriate to the lesser ionic radius of Cu^{2+} (0.71 \AA) compared to that of Zn^{2+} (0.74 \AA) [18]. The magnitude of intensity of the peaks turns into more strong and sharper by Cu-doping which is due to the crystallinity of the films being improved and grain size becoming larger. When Cu is substituted into $\text{Zn}_{0.98}\text{Mn}_{0.02}\text{S}$, the XRD peaks shows the appearance of new peaks at $2\theta \approx 27.92^\circ$ (corresponding to (100) plane hexagonal phase) and the peak corresponding to (200) plane. The emergence of additional peaks associated with hexagonal phases (marked as ☆) which indicating that both hexagonal and cubic (marked as ●) phases co-exist in a single sample. Generally, cubic phase of ZnS is thermodynamically stable phase and hexagonal wurtzite phase of ZnS is metastable phase at ambient condition. Therefore, the stable phase (cubic phase) noticed in $\text{Zn}_{0.98}\text{Mn}_{0.02}\text{S}$ is disturbed by Cu concentration which makes them metastable phase (co-existence of hexagonal and cubic phases). The observed phase transition is due nanosize effect [19] or tuning of morphology [20].

The signature of secondary phases after Cu substitution specifies that Cu would not only the substitute the Zn place but also exist as interstitial ions and or entered into

vacancies [21]. The peak intensity of (220)/(110) plane is gradually decreased by Cu-doping and finally flopped (almost) for ZCM-4. The average crystallite size is evaluated by carrying out by proper background correction from X-ray line broadening of the peaks of (111) plane using Debye-Scherrer's formula [22]:

$$\text{Average crystallite size } (D) = \frac{0.9\lambda}{\beta \cos\theta} \quad (1)$$

where, λ is the wave length of X-ray used (1.5408 \AA), β is the angular peak width at half maximum in radian along (111) plane, and θ is the Bragg's diffraction angle. The micro-strain (ϵ) developed in the nanocrystals are calculated using the formula [22].

$$\text{Micro-strain } (\epsilon) = \frac{\beta \cos\theta}{4} \quad (2)$$

where, λ is the wavelength of X-ray used (\AA), β is the angular peak width at half maximum in radian, and θ is the Bragg's diffraction angle.

The peak position (2θ), FWHM (β) value, d -value, cell parameter ' a ', average crystallite size (D) and micro-strain (ϵ) of $\text{Zn}_{0.98}\text{Mn}_{0.02}\text{S}$ and ZCM-2 and ZCM-4 are shown in Table 1. FWHM values of $\text{Zn}_{0.98}\text{Mn}_{0.02}\text{S}$ QDs decreased gradually with increase of Cu concentration which revealed the enrichment of crystallization. It is noticed from Table 1 that the average crystallite sizes are $\sim 17.5, 18.3$ and 19.3 \AA for Cu = 0, 2 and 4 %, respectively i.e., crystallite size is gradually increased by Cu concentration. Reddy et al. [21] illustrated the decrease of crystallite size after Cu = 3 at.% dopant concentration in $\text{Zn}_{0.97-x}\text{Cu}_x\text{Cr}_{0.03}\text{S}$ QDs due to the lattice disorder produced in the sample. In the present case, crystallite size is continuously increased which ignore the lattice disorder by Cu-doping except the phase (hexagonal and cubic) co-existence. The similar enhancement of crystallite size was perceived in the literature after co-doping Cu in ZnS with Cd [23] and Co [14]. The micro-strain of the samples is continuously decreased with increase of Cu concentration which is accountable for the augmentation of crystallite size and narrowing of diffraction peaks.

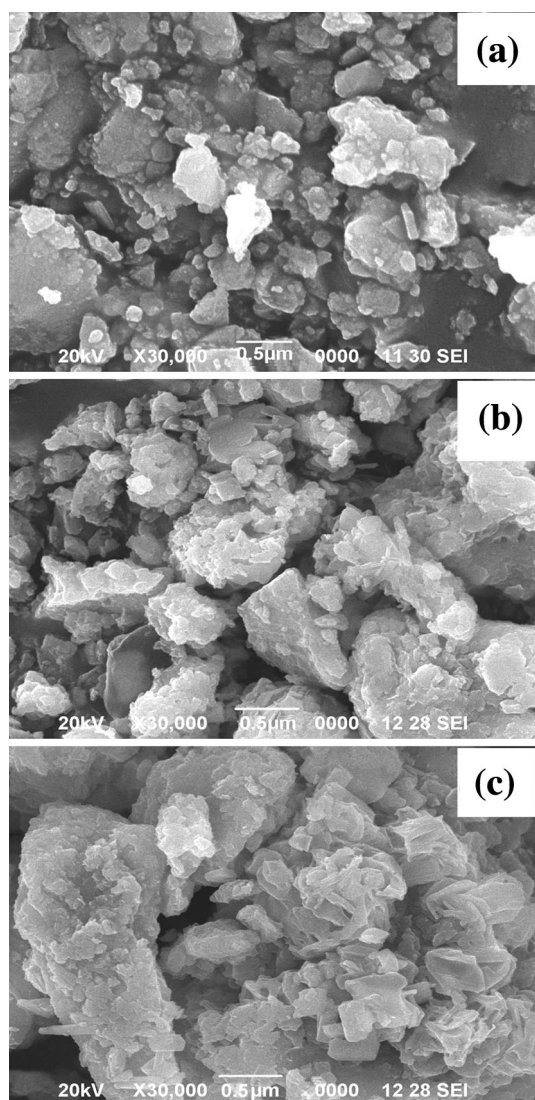
The interplanar distance ' d ' and lattice parameter ' a ' of ZCM-2 and ZCM-4 are always higher than $\text{Zn}_{0.98}\text{Mn}_{0.02}\text{S}$ QDs i.e., both are continuously decreased by Cu-doping. Since the ionic radius of Cu^{2+} ($\approx 0.71 \text{ \AA}$) is less than the ionic radius of Zn^{2+} (0.74 \AA), Cu^{2+} replaces Zn^{2+} substitutionally. Therefore, the diminishing of ' d ' and ' a ' are owing to the proper substitution of Cu^{2+} (which has lower ionic radius than Zn^{2+}).

3.2 SEM—Microstructural Study

The surface morphology of $\text{Zn}_{0.98-x}\text{Cu}_x\text{Mn}_{0.02}\text{S}$ ($x = 0, 0.02$ and 0.04) QDs is shown in Fig. 2. The SEM image of

Table 1 The peak position (2θ), full width at half maximum (FWHM, β) value, d -value, average crystallite size (D) and micro-strain (ϵ) along (111) plane of $\text{Zn}_{0.98}\text{Mn}_{0.02}\text{S}$, ZCM-2 and ZCM-4 quantum dots

Samples	Peak position (2θ) ($^\circ$)	FWHM ($^\circ$)	$d_{(111)}$ (\AA)	Lattice parameter, a (\AA)	Crystallite size (D) (\AA)	Micro-strain (β) $\times 10^{-3}$
$\text{Zn}_{0.98}\text{Mn}_{0.02}\text{S}$	28.58	4.69	3.121	5.406	17.5	19.83
ZCM-2	29.15	4.49	3.061	5.303	18.3	18.96
ZCM-4	29.43	4.26	3.033	5.253	19.3	17.98

**Fig. 2** Scanning electron microscope images of **a** $\text{Zn}_{0.98}\text{Mn}_{0.02}\text{S}$, **b** ZCM-2 and **c** ZCM-4 QDs

$\text{Zn}_{0.98}\text{Mn}_{0.02}\text{S}$ QDs (Fig. 2a) shows the formation of nearly spherical particles. Figure 2b shows the surface morphology of ZCM-2 where spherical shape of the particles was slightly turned into rod-shape particles. The observed small particles can be easily seen adhere to the surface of the big particles. SEM images contains the size of the secondary

particles only which consist of primary particles in nano-size. The conversion of rod-shape was enhanced by Cu-doping (Fig. 2c, $\text{Cu} = 0.04$) and also higher Cu concentration increases the agglomerations of particles. The size derived from XRD pattern is different from SEM images because XRD shows crystallite size but SEM shows the agglomerated particles. During chemical reaction (synthesis), nano-clusters aggregate into larger secondary spherical particles and secondary spherical particles further collide and merge with each other to form multimers (e.g., dimers, trimers, etc.). Due to agglomeration of grains it is not possible to specify the exact size and the grain sizes ranging from 3 to 8 nm.

Datta et al. [24] reported that with increasing the Cu concentration (after $\text{Cu} = 1 \text{ mol}\%$) in ZnS, the wurtzite ZnS nanorods gradually phase transformed to cubic structure and the growth direction of the nanorods changed along the (111) plane. Wang et al. [20] also described the phase change in ZnS nano-belts and explained it based on tuning of morphology. In our case, cubic phase of ZnS is tuned towards hexagonal phase by Cu-doping i.e., morphology diminishes stability by tuning surface-energy density.

3.3 EDX—Compositional Analysis

The elemental composition analysis of $\text{Zn}_{0.98-x}\text{Cu}_x\text{Mn}_{0.02}\text{S}$ ($x = 0, 0.02$ and 0.04) QDs is carried out by EDX. Figure 3 shows the EDX spectra of $\text{Zn}_{0.98}\text{Mn}_{0.02}\text{S}$ and ZCM-2 and ZCM-4. The quantitative atomic percentage of the compositional elements such as Zn, S, Mn and Cu in $\text{Zn}_{0.98-x}\text{Cu}_x\text{Mn}_{0.02}\text{S}$ ($x = 0, 0.02$ and 0.04) are presented in Table 2.

Figure 3 shows the well defined peaks corresponding to Zn, S, Mn and Cu in all the samples. The amount of Cu and Mn present in the samples was confirmed from Table 2; however, it was observed that the proportion of experimentally doped Cu and Mn in the ZnS is a little lesser than that was added in the reaction. It is noticed from Table 2 that the atomic percentage of Mn and S is more or less stable, but concentration of Zn is decreased and atomic percentage of Cu is increased. The increasing Cu atomic percentage clearly exposes that the Cu^{2+} ions are

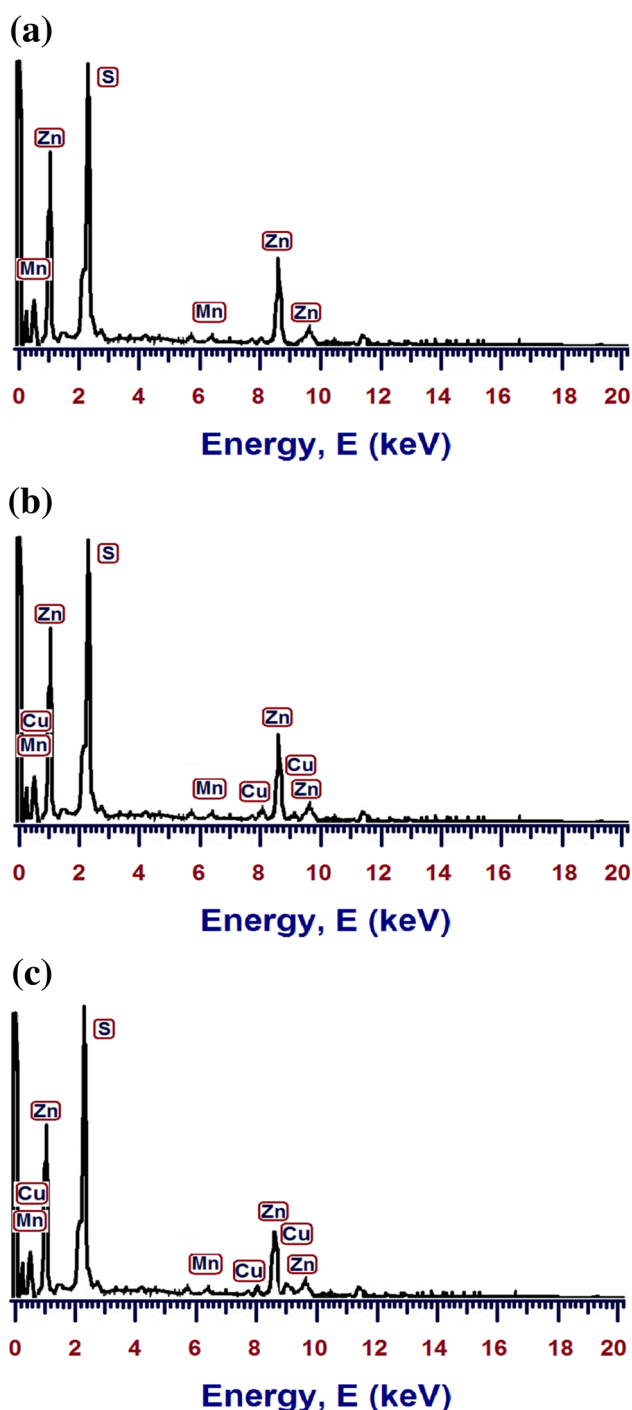


Fig. 3 Energy dispersive X-ray (EDX) spectra of **a** $\text{Zn}_{0.98}\text{Mn}_{0.02}\text{S}$, **b** ZCM-2 and **c** ZCM-4 QDs

incorporated appropriately in the Mn doped ZnS [25]. No other elements found from Fig. 3 authenticate the purity of the samples. $\text{Cu}/(\text{Zn} + \text{Mn} + \text{Cu})$ ratio is derived to be 1.76 and 3.86 % for $\text{Cu} = 2$ and 4 %, respectively. The obtained results are nearly equal to their stoichiometry within the experimental error.

3.4 Optical Studies

The examination of optical absorption and transmittance of the samples is the most important one to know the optical performance of quantum dots. Figure 4 illustrates the UV–Vis absorption and transmittance spectra of undoped $\text{Zn}_{0.98}\text{Mn}_{0.02}\text{S}$, ZCM-2 and ZCM-4 between from 300 and 600 nm at room temperature.

$\text{Zn}_{0.98}\text{Mn}_{0.02}\text{S}$ QDS exhibits an excellent absorption in the wavelength up to 330 nm which has a highest value around 308 nm at room temperature [26]. The wavelength of absorption edge shifted towards higher wavelength i.e., lower energy side by substitution of Cu into $\text{Zn}_{0.98}\text{Mn}_{0.02}\text{S}$ as shown in Fig. 4a. The present red shift explores the replacement of Zn by Cu in Zn–Cu–Mn–S lattice and also narrowing of band gap by Cu-doping [27]. The increment in crystal size is also another possible reason for the red shift of absorption edge. The intensity of absorption is enhanced at lower Cu concentration which supports the proper substitution of Cu^{2+} ions instead of Zn^{2+} ions. Further increase of Cu concentration decreases the absorption intensity and also shifts the absorption edge towards the lower wavelength (higher energy, i.e., blue shift) side. The decrease of absorption intensity can be attributed to defect states owing to the imperfections in lattice structure due to different sizes of Cu^{2+} , Mn^{2+} and Zn^{2+} . One more reason to decrease the absorption intensity is scattering of light by grain boundaries as well as Cu cluster which reflect the incident light [21].

Figure 4b shows the room temperature transmittance spectra of undoped $\text{Zn}_{0.98}\text{Mn}_{0.02}\text{S}$, ZCM-2 and ZCM-4 from 300 to 600 nm. All the samples have semi-transparent nature. The transmittance of the samples varied between 40 and 80 % where ZCM-4 exhibits higher transparency in visible region. Transmittance of the samples was improved by Cu-doping and all the samples have sharp increase of transmittance at UV region due to the inter-band transitions from valence band transitions towards the conduction band and the exhibit transparent in the visible region.

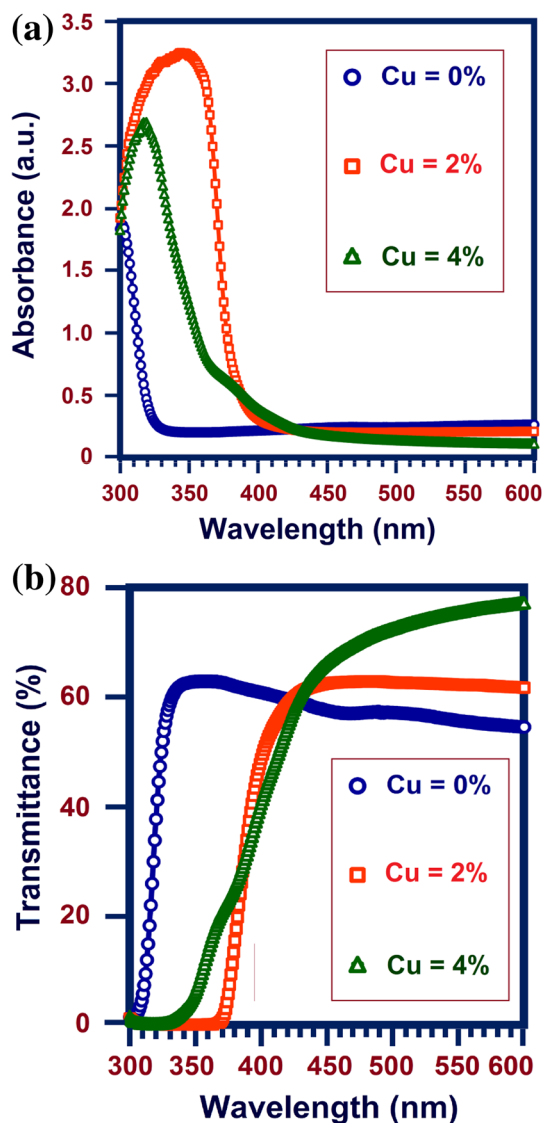
The optical band gap of undoped $\text{Zn}_{0.98}\text{Mn}_{0.02}\text{S}$, ZCM-2 and ZCM-4 can be calculated by using the Tauc's equation which demonstrates a relationship between absorption coefficient (α) and the incident photon energy ($h\nu$) of semiconductors as follows [22]:

$$\alpha h\nu = A (h\nu - E_g)^n \quad (3)$$

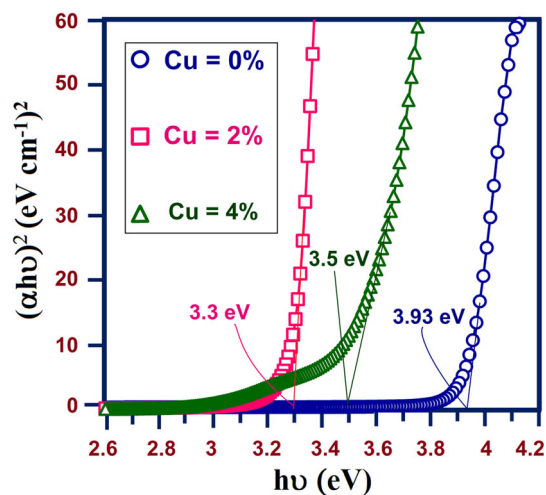
where, A is a constant, E_g is optical band gap of the material. In the present case, the exponent 'n' is taken as $1/2$ because of the direct allowed transition. The energy band gap (E_g) of samples can be obtained by plotting $(\alpha h\nu)^2$ versus $h\nu$ and extrapolating the linear portion of the absorption edge as shown in Fig. 5.

Table 2 The quantitative analysis of atomic percentage of the compositional elements presents in of $\text{Zn}_{0.98}\text{Mn}_{0.02}\text{S}$ ZCM-2 and ZCM-4 quantum dots using EDX analysis

Samples	Atomic percentage of the elements (%)				Mn/(Zn + Mn + Cu) ratio (%)	Cu/(Zn + Mn + Cu) ratio (%)
	Zn	S	Mn	Cu		
$\text{Zn}_{0.98}\text{Mn}_{0.02}\text{S}$	54.72	44.21	1.07	–	1.92	–
ZCM-2	53.81	44.16	1.05	0.98	1.88	1.76
ZCM-4	52.73	44.07	1.04	2.16	1.86	3.86

**Fig. 4** UV-visible **a** absorption spectra and **b** transmittance spectra of $\text{Zn}_{0.98-x}\text{Cu}_x\text{Mn}_{0.02}\text{S}$ ($x = 0, 0.02$ and 0.04) QDs from 300 to 600 nm

Hexagonal phase of ZnS has a bulk band gap of ~ 3.77 eV and cubic phase of ZnS exhibit an energy gap of ~ 3.72 eV at room temperature [28]. The derived energy gap of $\text{Zn}_{0.98}\text{Mn}_{0.02}\text{S}$ QD from Fig. 5 is 3.93 eV. This estimated band gap is slightly higher than that of bulk ZnS

**Fig. 5** The $(\alpha h\nu)^2$ versus $h\nu$ curves for the optical band gap determination of $\text{Zn}_{0.98-x}\text{Cu}_x\text{Mn}_{0.02}\text{S}$ ($x = 0, 0.02$ and 0.04) QDs

and observed blue shift of energy gap may be ascribed to quantum confinement effects. The energy gap of ZCM-2 is found to be 3.3 eV. The decrease in band gap after Cu-doping is associated with the structural (Fig. 2) and phase modification (Fig. 1). The introduced Cu brings some extra energy levels in the ZnS nearer to the valence band edge, with a consequent reduction of the energy associated with direct transition. And also the diminish of energy gap by Cu-doping can be explained by direct energy transfer between semiconductor excited states and 3d levels of the Cu^{2+} ions, that are coupled by energy transfer process [29]. The increase of crystallite size (lies within the few nanometers range) with increase in Cu content ($\text{Cu} = 2\%$) as noticed from Table 1 also support the narrowing of band gap. The similar narrowing of energy gap was reported after co-doping of Cu^{2+} in ZnS with dopants like In [30].

After attaining the minimum band gap (3.3 eV) at ZCM-2, band gap increases with the addition of Cu doping ($E_g \approx 3.5$ eV for $\text{Cu} = 4\%$). The noticed rise of band gap after $\text{Cu} = 0.02$ possibly due to filling up of high energy conduction band by the additional charge carriers provided by Zn/Cu/Mn atoms. The produced carriers by impurity atoms make the blue shift of band gap by blocking the low energy transitions.

3.5 Fourier Transforms Infra Red (FTIR) Studies

FTIR is one of the vital methods to investigate the chemical elements and bonding in the substance, recognize and differentiate the organic species of the substance. The room temperature FTIR spectra of undoped $\text{Zn}_{0.98}\text{Mn}_{0.02}\text{S}$, ZCM-2 and ZCM-4 are carried out in the wave number range from 400 to 4000 cm^{-1} and presented in Fig. 6. The wide absorption peaks around $3300\text{--}3400\text{ cm}^{-1}$ related to normal polymeric O–H stretching vibration, which specify the presence of water on the surface of the sample [31]. The spectral band obtained at 2338 cm^{-1} is associated with stretching vibration arising from the absorption of atmospheric CO_2 on the surface of the sample [19]. The observed vibration bands around 1400 cm^{-1} suggested the C–H bending [32]. Another absorption band about 1610 cm^{-1} is due to the H–O–H bending vibration of the water molecules [33]. The peaks noticed around 1016 cm^{-1} is due to the microstructure formation of the samples. The peak appears around 1024 cm^{-1} and the shift

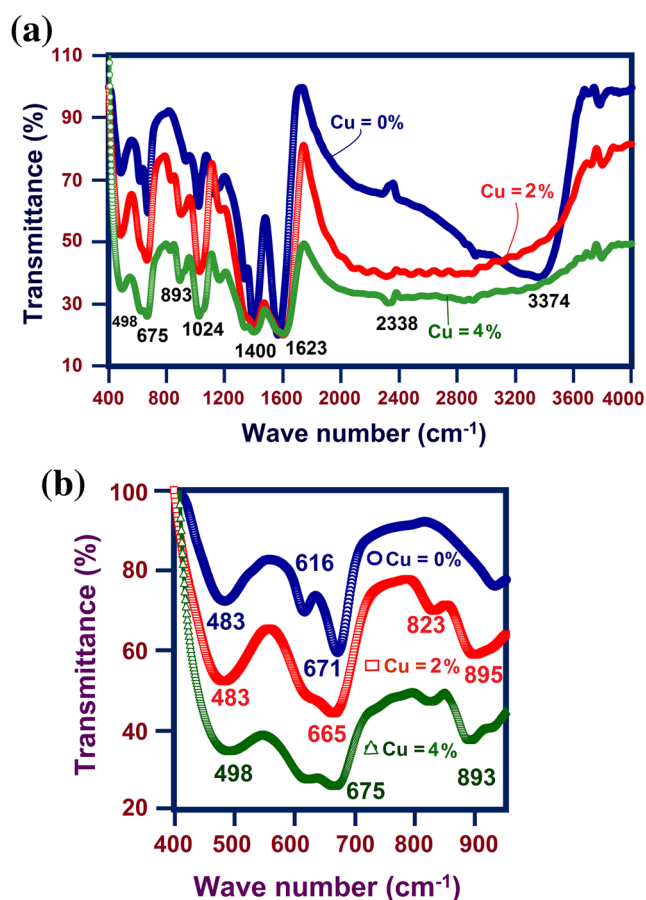


Fig. 6 FTIR spectra of $\text{Zn}_{0.98-x}\text{Cu}_x\text{Mn}_{0.02}\text{S}$ ($x = 0, 0.02$ and 0.04) QDs **a** in the wave number range from 400 to 4000 cm^{-1} at room temperature and **b** high resolution FTIR spectra from 400 cm^{-1} to 1000 cm^{-1}

of its position towards higher wave number side implying that both Mn and Cu were effectively entered into ZnS host.

Figure 6b demonstrates the magnified room temperature FTIR spectra of undoped $\text{Zn}_{0.98}\text{Mn}_{0.02}\text{S}$, ZCM-2 and ZCM-4 between 400 and 4000 cm^{-1} . The low magnitude bands appeared around $880\text{--}920\text{ cm}^{-1}$ represents the defect related microstructural formation which is increased by Cu-doping. The detected absorption bands around $671\text{--}675$ and $483\text{--}498\text{ cm}^{-1}$ are owing to the Zn–S stretching vibrations. The attained absorption bands are in excellent concurrence with the previous literatures [34, 35].

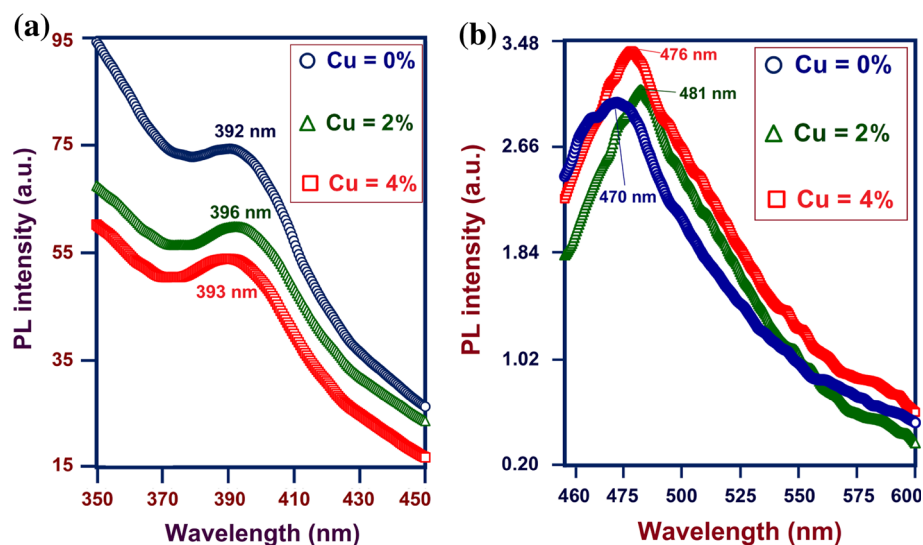
3.6 Photoluminescence (PL) Spectra

To investigate the light-emitting property of undoped $\text{Zn}_{0.98}\text{Mn}_{0.02}\text{S}$, ZCM-2 and ZCM-4, room temperature PL spectroscopy were carried out. Figure 7a illustrates room temperature PL spectra of the prepared samples between 350 nm and 450 nm and Fig. 7b shows the PL spectra from 455 to 600 nm .

Generally, the emission of pure ZnS originated from an electron band to band transition are in the ultraviolet region and the visible luminescence should usually arising from impurity or native defect levels. It is noticed from Fig. 7a that $\text{Zn}_{0.98}\text{Mn}_{0.02}\text{S}$ QDs have strong emission band centered at 392 nm corresponding to UV emission. The intensity of UV emission is maximum for undoped $\text{Zn}_{0.98}\text{Mn}_{0.02}\text{S}$ which is gradually decreased by the addition of Cu concentration. In addition to decrease in intensity, the band position of UV emission is slightly shifted to higher wavelength side (red shift). The possible reason for both decrease in intensity and red shift of UV band is the higher crystallize size where the enhanced crystal absorb and release at longer wavelengths relative to smaller size [36]. Another possible reason for decrease in UV intensity in Cu-doped sample is the formation luminescence centers by Cu^{2+} ions which trap electrons and holes and enhance the non-radiative recombination process [21].

Figure 7b shows that $\text{Zn}_{0.98}\text{Mn}_{0.02}\text{S}$ QDs exhibit a broad emission band peaked at 470 nm . The observed blue band emission can be attributed to self-activated sulfur defects and/or interstitial lattice defects. The defect related blue emission is possible as a consequence of recombination of free charge carriers at defect sites [37]. Mn, Cu co-doped ZnS exhibit a slight red shift of blue band emission in the wavelength range $470\text{--}481\text{ nm}$. The similar single broad blue band emission at about 480 nm was reported by Khosravi et al. [38] in Cu-doped ZnS. Cu-doped $\text{Zn}_{0.98}\text{Mn}_{0.02}\text{S}$ QDs comprise a larger surface atom ratio and hence higher defect states at the surfaces of the samples. This defect related recombination of charge carriers is responsible for blue band emission. The observed blue

Fig. 7 Room temperature photoluminescence spectra of $Zn_{0.98-x}Cu_xMn_{0.02}S$ ($x = 0, 0.02$ and 0.04) QDs **a** from 350 to 450 nm and **b** from 460 to 600 nm using 330 nm line of Xe excitation source



band emission is the feature of Cu^{2+} ion and is ascribed to the transition of the electrons from the (surface states) conduction band of ZnS to the ‘ t_2 ’ levels of Cu impurities [39]. The formation of more and more defect states and luminescent centers in ZnS structure by Cu-doping enhance the blue band intensity.

4 Conclusions

Followings are the conclusions drawn present investigations:

- $Zn_{0.98-x}Mn_{0.02}Cu_xS$ ($x = 0, 0.02$ and 0.04) QDs have been successfully synthesized by co-precipitation method.
- XRD patterns confirmed the phase transition from cubic, exhibited in $Zn_{0.98}Mn_{0.02}S$ QD to fusion of hexagonal and cubic phase by Cu substitution into $Zn_{0.98}Mn_{0.02}S$ which is discussed by change in size and tuning of morphology.
- The observed small shift in peak position along (111) plane and the diminishing of interplanar distance and lattice constant confirmed the the proper substitution of Cu and Mn in ZnS.
- Cubic phase of ZnS was tuned towards hexagonal phase by Cu-doping i.e., morphology diminishes stability by tuning surface-energy density.
- The extensive tuning of band gap between 3.3 and 3.93 eV by Mn-doping and Cu co-doping is useful in opto-electronic device applications.
- FTIR confirmed the presence of Mn and Cu in ZnS QDs.
- PL spectra showed two distinct emission bands, UV emission around 392–396 nm due to band to band

transition and defect related blue emission around 470–481 nm.

- The change in intensity and peak position of UV and blue emission was discussed based on crystallite size and formation of defect states by Cu-doping.

References

1. C.J. Murphy, *Anal. Chem.* **74**, 520A–526A (2002)
2. P.C. Kuo, H.W. Wang, S.Y. Chen, *J. Ceram. Soc. Jpn.* **114**, 918–922 (2006)
3. P.V. Kamat, *J. Phys. Chem. C* **112**, 18737 (2008)
4. W.S. Zou, D. Sheng, X. Ge, J.-Q. Qiao, H.-Z. Lian, *Anal. Chem.* **83**, 30–37 (2011)
5. B.B. Srivastava, S. Jana, N. Pradhan, *J. Am. Chem. Soc.* **133**, 1007–1015 (2011)
6. R.N. Bhargava, *J. Lumin.* **70**, 85–94 (1996)
7. P.K. Sharma, R. Nass, H. Schmidt, *Opt. Mater.* **10**, 161–169 (1998)
8. U. Sohling, G. Jung, D. Saenger, S. Lu, B. Kutsch, M. Mennig, *J. Sol-Gel. Sci. Technol.* **13**, 685–689 (1998)
9. J. Huang, Y. Yang, S. Xue, B. Yang, S. Liu, J. Shen, *Appl. Phys. Lett.* **70**, 2335–2337 (1997)
10. B. Vaidhyanathan, C.P. Kumar, J.L. Rao, K.J. Rao, *J. Phys. Chem. Solids* **59**, 121–128 (1998)
11. R.P.S. Chakradhar, B.M. Nagabhushana, G.T. Chandrappa, K.P. Ramesh, J.L. Rao, *J. Chem. Phys.* **121**, 10250–10259 (2004)
12. R.N. Bhargava, D. Gallagher, X. Hong, A. Nurmiko, *Phys. Rev. Lett.* **72**, 416–419 (1994)
13. P. Sakthivel, S. Muthukumar, M. Ashokkumar, *J. Mater. Sci.* **26**, 1533–1542 (2015)
14. P. Yang, M. Lu, G. Zhou, D. Yuan, D. Xu, *Inorg. Chem. Commun.* **4**, 734–737 (2001)
15. N. Uzar, S. Okur, M.C. Arikan, *Sens. Actuators, A* **167**, 188–193 (2011)
16. M. Geszke, M. Murias, L. Balan, G. Medjahdi, J. Korczynski, M. Moritz, J. Lulek, R. Schneider, *Acta Biomater.* **7**, 1327–1338 (2011)

17. J.C. Lee, N.G. Subramaniam, J.W. Lee, T.W. Kang, *Appl. Phys. Lett.* **90**, 262909 (2007)
18. F.J. Owens, L. Gladczuk, R. Szymczak, P. Dluzewski, A. Wisniewski, H. Szymczak, A. Golnik, Ch. Bernhard, Ch. Niedermayer, *J. Phys. Chem. Solids* **72**, 648–652 (2011)
19. S.B. Qadri, E.F. Skelton, D. Hsu, A.D. Dinsmore, J. Yang, H.F. Gray, B.R. Ratna, *Phys. Rev. B* **60**, 9191 (1999)
20. Z. Wang, L.L. Daemen, Y. Zhao, C.S. Zha, R.T. Downs, X. Wang, Z.L. Wang, R.J. Hemeley, *Nat. Mater.* **4**, 922–927 (2005)
21. D.A. Reddy, G. Murali, B. Poornaprakash, R.P. Vijayalakshmi, B.K. Reddy, *Appl. Surf. Sci.* **258**, 5206–5211 (2012)
22. S. Anandan, S. Muthukumar, *Microstructural. J. Mater. Sci.* **26**, 4298–4307 (2015)
23. P. Yang, M. Lu, D. Xu, D. Yuan, C. Song, *J. Phys. Chem. Solids* **64**, 155–158 (2003)
24. A. Datta, S.K. Panda, S. Chaudhuri, *J. Solid State Chem.* **181**, 2332–2337 (2008)
25. M. Ashokkumar, S. Muthukumar, *J. Mater. Sci.* **26**, 1225–1233 (2015)
26. C.M. Huang, L.C. Chen, G.T. Pan, T.C.K. Yang, W.S. Cheng, K.W. Cheng, *Mater. Chem. Phys.* **117**, 156–162 (2009)
27. P. Yang, M. Lü, D. Xü, D. Yuan, G. Zhou, *Appl. Phys. A* **73**, 455–458 (2001)
28. Y.Q. Li, J.A. Zapien, Y.Y. Shan, S.T. Lee, *Appl. Phys. Lett.* **88**, 013115–013117 (2006)
29. W.B. Sang, Y.B. Qian, J. Min, D. Li, L. Wang, W. Shi, L. Yinfeng, *Solid State Commun.* **121**, 475–478 (2002)
30. P. Yang, M.K. Lu, C.F. Song, D. Xu, D. Yuan, X.F. Cheng, G.J. Zhou, *Opt. Mater.* **20**, 141–145 (2002)
31. S. Ummartyotin, N. Bunnak, J. Juntaro, M. Sain, H. Manuspiya, *Solid State Sci.* **14**, 299–304 (2012)
32. N.R. Pavaskar, C.A. Menezes, A.B.P. Sinha, *J. Electrochem. Soc.* **124**, 743–748 (1977)
33. B. Malinowska, M. Rakib, G. Durand, *Solar Energy Mater. Solar Cells* **86**, 399–419 (2005)
34. B.S. Rema Devi, R. Raveendran, A.V. Vaidyan, Pramana, *J. Phys.* **68**, 679–687 (2007)
35. Y. Tong, Z. Jiang, C. Wang, Z.Y. Xin, S. Hong, Liu, *Mater. Lett.* **62**, 3385–3387 (2008)
36. W. Hoheisel, V.L. Colvin, C.S. Johnson, A.P. Alivisatos, *J. Chem. Phys.* **101**, 8455–8460 (1994)
37. D. Denzler, M. Olschewski, K. Sattler, *J. Appl. Phys.* **84**, 2841–2845 (1998)
38. A.A. Khosravi, M. Kundu, L. Jatwa, S.K. Deshpande, U.A. Bhagwat, M. Sastry, K. Kulkarni, *Appl. Phys. Lett.* **67**, 2702 (1995)
39. A. Datta, S. Biswas, S. Kar, S. Chaudhuri, *J. Nanosci. Nanotechnol.* **10**, 3670–3676 (2007)